Soft Matter

PAPER

View Article Online
View Journal

Cite this: DOI: 10.1039/d5sm00869g

Stretching and debonding of adhesive fibril

Krupal Patel, *[a] Matteo Ciccotti [b] and Etienne Barthel[b]

Received 27th August 2025,
Accepted 4th January 2026

DOI: 10.1039/d5sm00869g

rsc.li/soft-matter-journal

In pressure-sensitive adhesive (PSA) tapes, adhesive failure is often accompanied by cavitation and fibrillation. In this paper, we focus specifically on fibrillation. We model the behavior using a single fibril (mono-fibril) configuration with the axisymmetric boundary conditions. Using the finite element method, we simulate the mono-fibril with varying aspect ratios using hyperelastic models such as Arruda–Boyce and Yeoh. First, we explain why the deformation of these fibrils is not purely uniaxial. We then analyze the normalized force–stretch response using appropriate scaling models. Then we examine the impact of changing strain-hardening, inter-fibrillar distance, and bulk modulus on the fibril response. Following this, we investigate fibril debonding using parameters of the Yeoh model fitted to the uniaxial rheological experimental data from two PSA tapes, referred to as PSA types 6A and 6B. Based on this analysis, we derive the power laws for debonding stretch and debonding force for both PSA types. Finally, we compare our findings with experimental data on mono-fibril debonding from the literature.

1 Introduction

Let us first consider the peeling experiment of PSA tapes, in which a commercial tape or custom-made tape is peeled from a substrate such as glass, polydimethylsiloxane (PDMS), or any other surface. Initially, the relatively soft adhesive layer is sandwiched between the stiff backing and the substrate, and gradually, it can be peeled from the surface by various means. In this simple experiment, the peel force can be measured by a dead weight as in Ciccotti *et al.*[1]

The pioneering work was by Kaelble[2] who uncovered the theory of peeling by an analytical method. Kaelble's model attempts to describe the cohesive zone by assuming the adhesive layer to be a viscoelastic foundation. It differs from the singularity-based approach of Linear Elastic Fracture Mechanics extended to soft solids by Rivlin *et al.*[3]

During the peeling of a pressure-sensitive adhesive (PSA), the adhesion energy Γ (the work that should be provided to peel a unit tape area) is several orders of magnitude above the thermodynamic Dupré surface energy Γ_0 between the adhesive and the underlying substrate. This demonstrates the dominant role of energy dissipation. In the slow steady-state regime, Γ is highly dependent on the temperature T and the peeling rate V.

$$\Gamma = \Gamma_0[1 + \Phi(T, V)] \quad (1)$$

$$= \Gamma_0 + \Gamma_D \quad (2)$$

where Γ_0 is the intrinsic fracture energy and Φ is a factor to account for the dissipative losses which depend on velocity V and temperature T.[4–8]

Further experimental work demonstrated that the adhesion energy depends not only on linear rheology[4–8] but also on nonlinear rheology.[9,10] Villey *et al.*[11] developed new tools that highlighted that fibril stretching within the cohesive zone is central to energy dissipation during steady-state peeling of PSAs. Chopin *et al.*[10] confirmed that non-linear rheological responses such as strain hardening and strain softening govern the peeling energy which had previously been modeled using linear viscoelastic models.[12–14]

At the heart of these processes lies the fibril debonding problem. Fibril debonding is the key missing ingredient in modeling the adherence energy of PSA tapes, according to Chopin *et al.*[10] During peeling or a probe-tack test, cavitation initiates voids in the adhesive layer, which translate into fibrils that undergo elevated nonlinear, rate-dependent deformation before detachment from the substrate.[15–26] However, accurate modeling of fibrillation and cavitation is difficult. Several studies have attempted to simulate the mechanical response of the adhesive using different approaches.[27–33] This fibrillation dissipates large amounts of energy, explaining the high values of Γ that are observed. While recent studies have explored fibril dynamics in detail, a general predictive model that quantitatively links fibril debonding to adhesion energy remains lacking. Developing such a framework is therefore key to understanding PSA performance and guiding the design of advanced adhesives.

Krishnana *et al.*[34] presented the numerical study of the large deformation of soft elastic material that is modeled as a

[a] Department of Engineering Science, University of Oxford, Oxford, OX1 3PJ, UK. E-mail: krupalpatel12@hotmail.com
[b] Soft Matter Sciences and Engineering Lab, ESPCI Paris, PSL University, CNRS, Sorbonne Université, 75005 Paris, France

half-space and is in adhesive contact with a rigid cylindrical flat punch. They considered the material of the half-space to be Neo-Hookean and gave results for non-slip and frictionless boundary condition. A more realistic problem occurs when the soft layer is sandwiched between the stiff half-space and stiff punch, which is investigated in the present study using the material models involving strain hardening. In a recent article by Duigou-Majumdar *et al.*,[35] studied fibril debonding from the PDMS pillar. In this study, they performed experiments showing the detachment of the tape from the top surface of a single micrometer-scale pillar of PDMS elastomer. At a constant displacement rate, the pillar and the adhesive separate, resulting in the generation of a mono-fibril of adhesive material. They provide the power laws for the maximum force and the critical elongation of the fibril at debonding as a function of fibril diameter obtained experimentally for the commercial double-sided acrylic adhesive tape. However, their mathematical model is based on an extension of linear theory to describe the phenomenon of nonlinear fibril debonding.

In this study, we will focus on modeling the nonlinear elastic response of the mono-fibril. The paper is divided into four sections: Introduction, Finite Element Method, Results, and Summary and discussion. In the subsequent section, we will define the problem statement, and in the later sections, we will discuss the results and finish with the concluding remarks.

2 Finite element method

Let us first consider a SEM image of the fibrillation captured by X. Morelle and B. Bresson at SIMM Lab, ESPCI Paris in Fig. 1a.

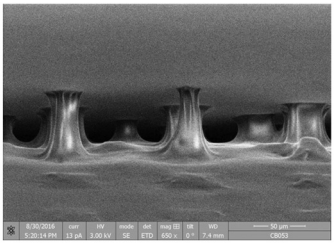

(a) SEM view of adhesion rupture of a PSA tape, showing fibrillation (X. Morelle and B. Bresson)

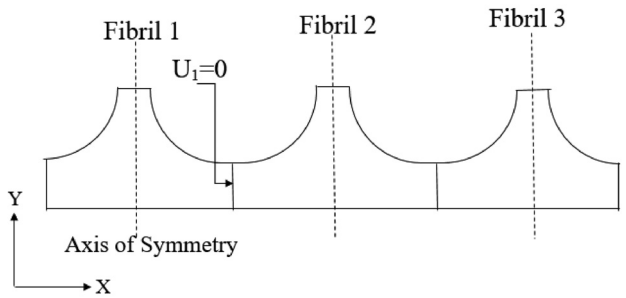

(b) Schematics of fibrils showing boundary conditions

Fig. 1 Fibrillation.

We made simple schematics in Fig. 1b out of the complex fibrillation process as seen in Fig. 1a. In our model, we use the axisymmetric boundary condition to simplify the finite element calculations and reduce our task to simulating a 2D section of a single fibril instead of several fibrils taken in 3D, as shown in the image of adhesion rupture. The interaction with the other fibrils is approximated by imposing the boundary conditions $U_r = 0$ on the periphery of the domain, as can be observed in Fig. 2, which is not the periodic boundary condition $U_1 = 0$ as shown in Fig. 1b because our simulation domain is axisymmetric. The geometric parameters for the initial configuration of the fibril confined between the substrate and the backing are described in Fig. 2, where '*a*' is the radius of the fibril, '*t*' is the thickness of the adhesive layer, '*b*' is the half of the inter-fibrillar distance and the fibril density is $\Phi = \frac{a^2}{b^2}$.

We used ABAQUS to simulate the fibril. We utilized the Arruda–Boyce[36] and Yeoh[37] model for simulating the nonlinear elastic response of the Fibril. We put the initial crack at the interface between the unindented part of the soft adhesive layer and the rigid backing or stiff punch in ABAQUS, which means that at the interface, the nodes are not connected, as depicted in Fig. 2 as a crack. To calculate the energy release rate, we employ the *J*-integral. To tackle the singularity at the tip of the crack, a spiderweb-type mesh was used. With such a mesh, the *J*-integral can be calculated over the concentric paths surrounding the node defined as the crack tip. The *J*-integral value is taken on the contour number 100. When Poisson's ratio is close to 0.5, the bulk modulus approaches infinity. Under nearly incompressible conditions, any small error in the predicted volumetric strain will appear as a large error in the hydrostatic

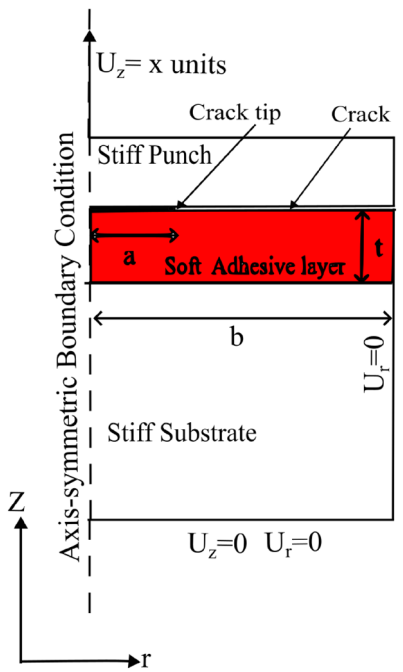

Fig. 2 Geometry and boundary conditions for fibril simulations.

pressure and subsequently in the stresses. This error will, in turn, also affect the displacement prediction since external loads are balanced by the stresses, and may result in displacements very much smaller than they should be for a given mesh. This is called locking, or no convergence at all. To overcome these difficulties, a mixed displacement-pressure formulation was developed that is available in the form of hybrid elements in ABAQUS. Hence, hybrid and reduced integration type elements (CAX4RH and CAX3H) are used to take care of the Poisson's ratio, which is close to 0.5 in the case of an incompressible adhesive layer.[38]

In the first part of the Results section, we discuss fibril stretching by normalizing it with the uniaxial stretching response and explain the behavior observed in the force–stretch curves using scaling models. We then examine the impact of varying the strain-hardening behavior in the material model, as well as the effect of interfibrillar distance in the fibril geometry. In addition, we investigated the influence of the bulk modulus on fibril deformation. In the final part, we focus on fibril debonding employing *J*-integrals within the fibril simulations.

3 Results

Parameters for the simulation using Arruda–Boyce model are given in the Table 1. We first tested the mesh sensitivity of our model. Representative results for a/t = 1.1 and λ = 3 are shown in Fig. S1(a) (SI) for 219 545 elements and in Fig. S1(b) (SI) for 329 682 elements. We find that the distribution remains constant except in the neighborhood of the singularity. Hence, our solutions are said to be grid-independent or robust with respect to the degree of mesh refinement. We also tested the grid independence at the other aspect ratios and details are available in Fig. S2(SI). To understand fibril deformation, it is interesting to compare the values of shear stress and hydrostatic pressure. Triaxiality is defined as the ratio of the von Mises stress to the absolute value of pressure. Representative results are shown in Fig. 3: it can be said that the stress triaxiality value is three at the center of the stretched fibril and decreases at the top and bottom.

3.1 Fibril stretching

We aim to compare the fibril stretching to the uniaxial stretching. We calculated fibril stretching for various aspect ratios a/t ranging from 0.12 to 2.2. In particular, we calculated the pulling force, which will be denoted F. We also calculated the force F_0 for uniaxial traction for the same material parameters. In Fig. 4, we plot F/F_0 *versus* λ for the different aspect ratios. These results show that the force needed to draw the fibril from a flat soft

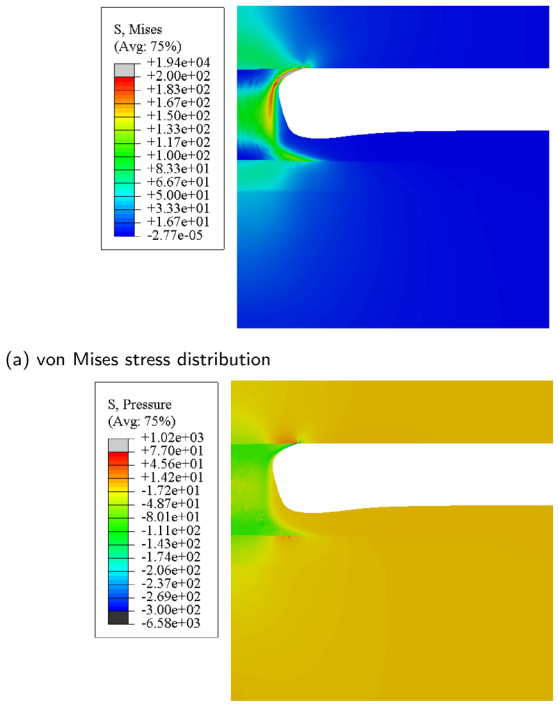

(a) von Mises stress distribution

(b) Pressure distribution

Fig. 3 Fibril simulations for a/t = 2.2, λ_L = 2, λ = 3. Shear and pressure distribution.

film is larger than the force to extend cylindrical fibrils by a factor of 3 to 14 depending on the value of aspect ratio. The small strain values of F/F_0 are shown in Fig. 5 and are seen to first decrease with a/t and then increase again. The small a/t regime can easily be explored by hand-waving arguments. For a flat-punch indenting a homogeneous half-space, the force in the linear regime is given by the following equation:

$$F \sim Ea\delta \tag{3}$$

and the uniaxial fibril force scales according to:

$$F_0 \sim E\frac{a^2}{t}\delta \tag{4}$$

Hence,

$$\frac{F}{F_0} \sim \frac{t}{a} \tag{5}$$

where $a \ll t$ and $\delta \ll a$. It can be seen in Fig. 5 that when $a \ll t$, the evolution of F/F_0 follows the scaling argument according to eqn (5), at a very small strain, and it is the intercept of F/F_0 with the vertical axis in Fig. 4a which represents the ratio of linear

Table 1 Parameter for simulations using Arruda–Boyce model: Poisson ratio of the soft layer = 0.4999

Parameter for simulations			
Name	Modulus of rigidity	Compliance of compressibility	Locking stretch
Rigid substrate and backing	μ_2 = 1000 MPa	D_2 = 0.0001 MPa^{-1}	λ_{L_2} = 3
Soft layer	μ_1 = 1 MPa	D_1 = 0.0001 MPa^{-1}	λ_{L_1} = 2

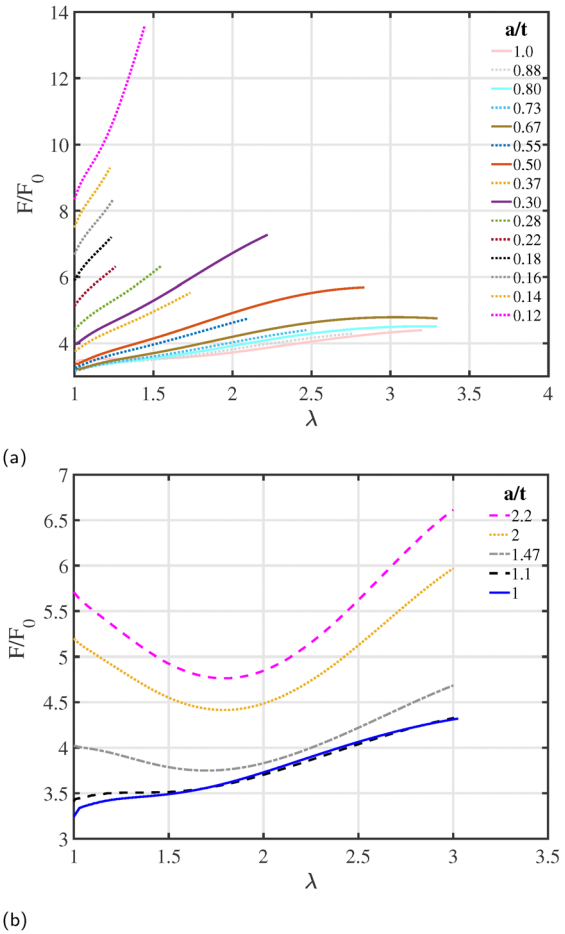

Fig. 4 Normalised force in the fibril simulations for (a) $a \leq t$ and (b) $a \geq t$ using the Arruda–Boyce model: $\mu_{rigid}/\mu_{soft} = 10^3$, $\lambda_L = 2$, $a = 1.1$ mm, $b = 10$ mm and t is varying.

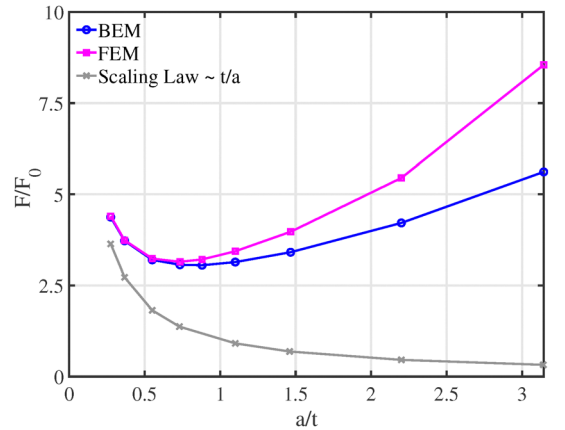

Fig. 5 Normalised force of the fibril in the linear regime: $\delta = 0.001$ mm.

contact stiffness. It can also be noticed that the boundary element method (BEM) matches the FEM exactly for $a \ll t$. For more details on the boundary element method, see our previous work.[39] Taking into account now larger stretches, for smaller a/t (Fig. 4a), we find that the ratio of F/F_0 increases roughly linearly with stretch as we move from small to moderate stretch. It is clear that as a/t decreases, the slope of this linear relation increases. In contrast, for a/t roughly larger than 1 (Fig. 4b), the evolution of F/F_0 with λ has a negative initial slope as the stretch increases from 1 to roughly 2. Above 2, there is a behavior change, and the slope becomes positive again. We also note that as a/t increases, the absolute value of the slope in the first regime, where we have a negative slope, increases. The same reasoning is true for the positive slope regime (that is, the stretch of 2 onward). This behavior can be explained qualitatively. Initially, when the adhesive layer is confined between the backing and the substrate, the shear energy is dominant, and the effective modulus is high. When the stretch increases, the confinement decreases, and the uniaxial part becomes dominant; hence, we have an initial negative slope. However, due to strain hardening, a positive slope is restored at the larger stretch.

We now give a more elaborate argument to explain the response at moderate strain and small a as seen in Fig. 4a. From Fig. 6a, it is clear that the affected area for this regime is less than the thickness of the adhesive layer in the small strain. Hence, it is near the half-space approximation as the thickness of the adhesive layer increases for the given radius. For flat-punch indenting over a homogeneous half-space, the force in the large strain regime ($a < \delta$) scales according to the following equation:

$$F \sim E\delta^2 \tag{6}$$

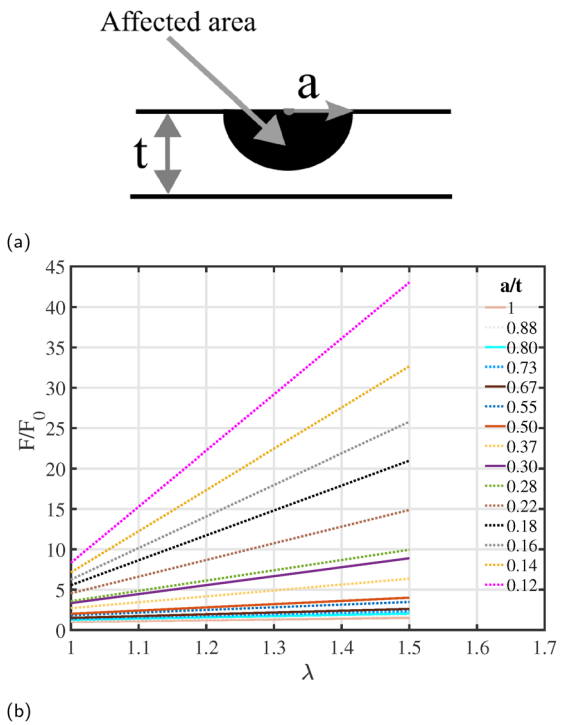

Fig. 6 (a) Kinematics for the cases where $a \ll t$ in the small strain regime (b) evolution of F/F_0 at small stretch for $a \ll t$ and various a/t values as predicted from eqn (5) and (7).

instead of eqn (3) because the volume affected by the deformation is now of size δ and not a. Hence,

$$\frac{F}{F_0} \sim \frac{\delta^2 t}{a^2 \delta} \sim \frac{t^2}{a^2}(\lambda - 1) \tag{7}$$

where $\lambda - 1 = \frac{\delta}{t}$. Eqn (7) qualitatively explains the linear behavior with λ at moderate strains and the increasing slope when $a \ll t$ in Fig. 4a.

In Fig. 4b, we see the initial negative slope of F/F_0 *versus* λ graph. Here, a qualitative argument is provided for this initial negative slope. It is based on the Neo-Hookean material model. In brief, the approximate expression for the elastic energy for uniaxial stretch is given by

$$W_{\text{uniaxial}} \sim a^2 t\mu\left(\lambda^2 + \frac{2}{\lambda} - 3\right) \tag{8}$$

For the fibril in the confined case (see Fig. 7a), we will show below that we have

$$W_{\text{fibril}} \sim a^2 t\mu\left[\left[\lambda_z^2 + \frac{2}{\lambda_z} - 3\right] + \left[\frac{a^2}{t^2}\left[\frac{1}{\lambda_z} - \frac{1}{\lambda_z^{3/2}}\right]^2\right]\right] \tag{9}$$

We can see that W_{fibril} consists of two terms. The first is due to uniaxial extension, and the second is due to shear. When a/t is large and λ is close to one, the shear part is dominant, but as λ increases, the uniaxial part takes over. Hence, we have a negative slope, as seen in Fig. 7b. Please visit Appendix A for the detailed derivation of eqn (9).

In Fig. 8, we plotted the slope of the force *vs.* stretch curve against the stretch using FEM results for fibril and uniaxial simulation. From the graph, we can say that the slope of the force for fibril is decreasing approximately till stretch of 1.7 and then it starts to increase while for the uniaxial case, it remains almost constant till the stretch of 2.5. Hence we can say that strain-hardening sets in earlier in the case of fibril than its corresponding uniaxial simulation for the high aspect ratio such as 2.2. Hence, we have positive slope in F/F_0 curve starting from stretch of 2 (when $a \gg t$), as seen in Fig. 4b.

3.2 Impact of strain hardening

Calculations were carried out with the parameters shown in Table 2 for the Arruda–Boyce model. We varied the locking stretch values from 2 to 5. From Fig. 9, we observe that the values of F/F_0 in the small strain for all the different locking stretches remain the same. In the large strain regime, as the value of the locking stretch increases, the value of F/F_0 decreases for a given value of the stretch. In Fig. 9, we plot the normalized force against the normalized strain. From this graph, we see that all the curves have the same slope, but the effect of strain hardening is visible by the shift of the curve according to the strain hardening value.

3.3 Impact of changing the inter-fibrillar distance

Here, we study the effect of changing the inter-fibrillar distance b on the F/F_0 ratio for the given a/t ratio. In Fig. 10, we plotted the F/F_0 *vs.* λ graph for the given a/t ratio and different b sizes. It

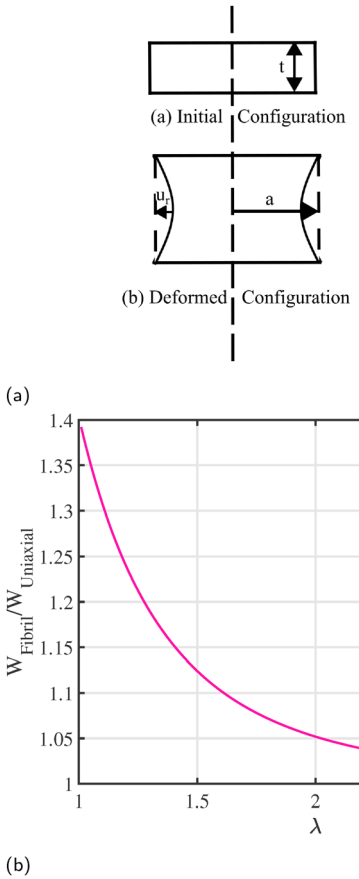

Fig. 7 (a) Kinematics for the cases where $a \gg t$ (b) Neo-Hookean material: Initial slope for a/t = 2.2 as predicted from eqn (9) and (8).

is observed that there is a moderate increase in the F/F_0 ratio when decreasing b and a moderate increase only appears for b/t ratio smaller than 2, *i.e.* for rather densely packed fibrils. Even in these conditions and despite the upward shift due to the lateral confinement, the evolution of the graph remains similar.

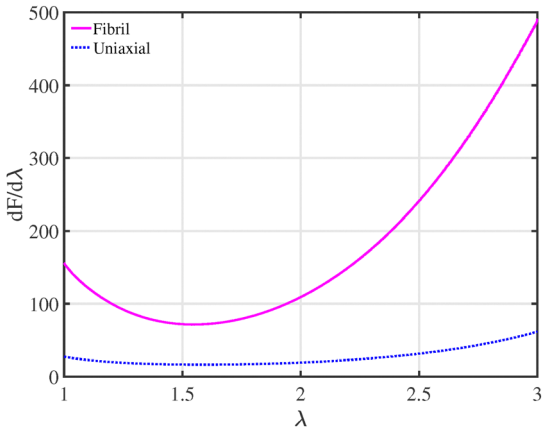

Fig. 8 Slope of force against stretch: Arruda–Boyce, a/t = 2.2, λ_L = 2, b = 10 mm: It gives an explanation of the positive slope in F/F_0 curve for aspect ratio: a/t = 2.2 starting from λ = 2.

Table 2 Parameter for simulations: Arruda–Boyce model

Parameter for simulations			
Name	Modulus of rigidity	Compliance of compressibility	Locking stretch
Rigid substrate	μ_2 = 1000 MPa	D_2 = 0.0001 MPa^{-1}	λ_{L_2} = 2, 3, 4, 5
Soft layer	μ_1 = 0.001 MPa	D_1 = 0.0001 MPa^{-1}	λ_{L_1} = 2, 3, 4, 5
Rigid backing	μ_2 = 1000 MPa	D_2 = 0.0001 MPa^{-1}	λ_{L_2} = 2, 3, 4, 5

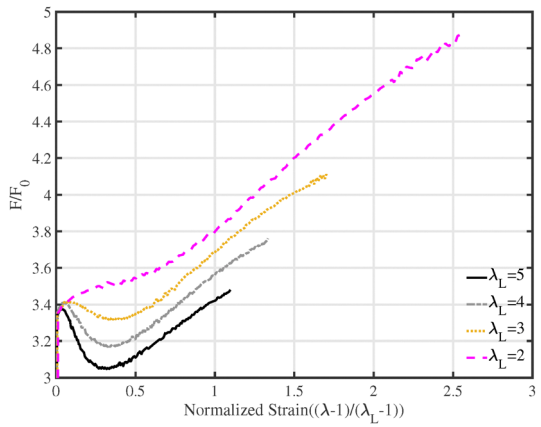

Fig. 9 Normalised force *vs.* Normalised strain for the different strain hardening value using the Arruda Boyce model: a/t = 1, μ_{rigid}/μ_{soft} = 10^6.

3.4 Change in the shape of the fibril due to change in the bulk modulus (*i.e.* compressibility)

Since confinement plays a role in the fibril response, it is interesting to study the impact of compressibility on the shape of the fibril. We used the standard Arruda–Boyce model with μ_1 = 1 MPa and an aspect ratio a/t = 1 and changed the bulk modulus from 2 to 2 × 10^4 MPa. We can observe in Fig. S3 (SI) from (a) to (e) that compressibility indeed plays a crucial role in determining the shape of the fibril. As we increase the bulk modulus for the same other parameters, the angle at the interface increases (θ_a = 100°, θ_b = 133°, θ_c = 140°, θ_d = 153°, θ_e = 150°), which seems directly related to the force required to pull these fibrils. Indeed, from Fig. 11, one can see that as the bulk modulus increases, the force necessary to stretch the fibril increases for a given value of the stretch. However, the initial increase of the force is visible but after a particular value of the bulk modulus, there is not much increase in the force at the specific stretch. It is clear that the angle θ increases monotonously when decreasing compressibility, as shown in Fig. S4(a) (SI). However, for the particular compressibility value, when we vary the applied stretch on the fibril, this angle first increases in the small strain and after a sudden increase, remains almost stable in the large strain as shown by Fig. S4(b) (SI).

In Fig. 12, we plotted the fibril force normalized by the force of the corresponding uniaxial simulation of the cylinder of the same patch diameter and thickness of the adhesive layer as that

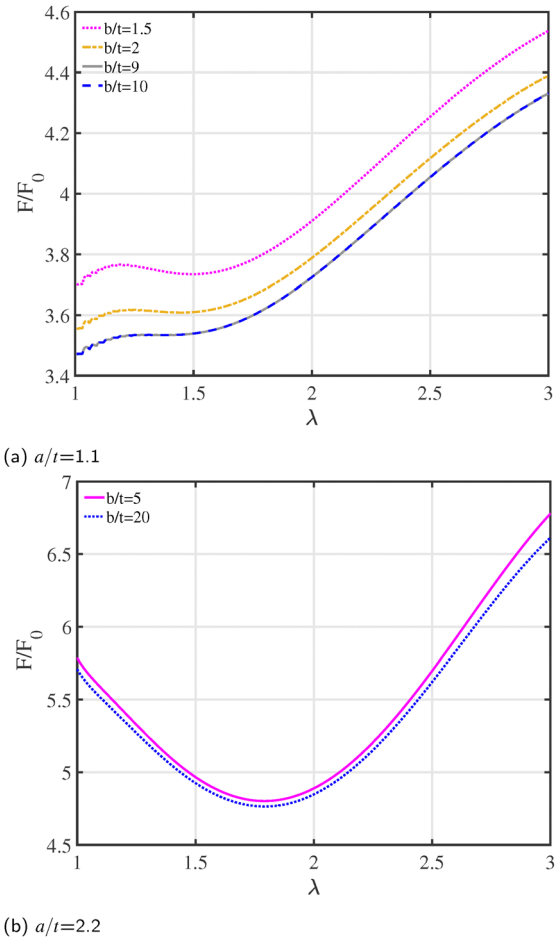

Fig. 10 F/F_0 *vs.* λ graph for the different b/t ratio for a given a/t: Arruda–Boyce, μ_{rigid}/μ_{soft} = 10^3, λ_L = 2. It explains the impact of half-interfibrillar distance: 'b'.

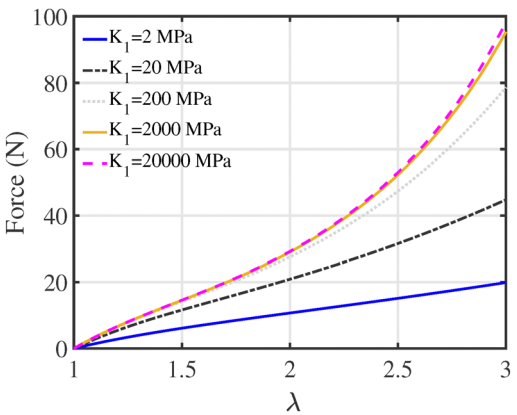

Fig. 11 Effect of change in bulk modulus on the force required to pull the fibril: Arruda–Boyce, a/t = 1, b = 10 mm, μ = 1 MPa, λ_L = 2.

of the fibril. We observe that as the bulk modulus decreases for the given shear modulus value, the force required to pull these fibrils decreases. And it costs less energy to pull the compressible fibril than pulling the relatively incompressible one. The

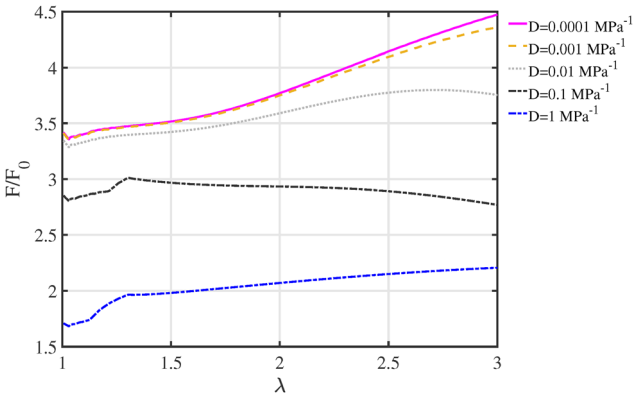

Fig. 12 Effect of change in Bulk Modulus on F/F_0 ratio: Arruda–Boyce, a/t = 1, b = 10 mm, μ = 1 MPa, λ_L = 2.

value of the F/F_0 factor also reduces with the reduction in the bulk modulus.

3.5 Fibril debonding

Chopin *et al.*[10] used two custom-made acrylate tapes made by 3M and labeled 6A and 6B in their work to model peeling adherence based on measurements of the extensional rheology. They measured the extensional data for several different strain rates. In this section, we characterize the same data to get the pertinent constitutive model parameters for our fibril simulations. We started data fitting with the Arruda–Boyce model, but the residuals after the fit procedure were too large. Hence, we eventually used the Yeoh model that provides a better fit for the two PSA tape as illustrated in Fig. S5 (SI). The fitting parameters are reported in Table 3.

We will now consider the consequences of the large-strain numerical simulations of the J-integral to discuss the consequences of the change of geometrical and material parameters on the debonding of the stretched fibril. In order to be close to the properties of our custom tapes 6A and 6B, we used the Yeoh model fit from Table 3 for the reference strain rate $\dot{\varepsilon}$ = 2 s^{-1}, which corresponds to a peeling speed of 0.1 mm s^{-1}. The parameters are reported in Table 4. We report in Fig. S9 (SI), J-integral simulated curves for several patch sizes and a constant tape thickness t = 20 μm as a function of stretch. We tested the mesh convergence of the J-integrals and force-stretch response and one can find that information in Fig. S6 and S8 (SI). In Fig. S7(SI), we tested the validity of ABAQUS's implementation of J-Integral using the finite-difference method.

By imposing the criterion of debonding based on $J = \Gamma$, where Γ represents the interfacial adhesion energy, we can determine the value of the critical stretch for debonding. Then we can evaluate by the force curve, as in Fig. S10 (SI), the corresponding critical force for debonding. Taking into account the constant value of Γ = 1, 4,[35] 10^{40} and 30 J m^{-2}, we can thus evaluate the dependence of both the critical force and the stretch as a function of the size a of the contact patch for the two custom PSA tapes (6A and 6B) as reported in Fig. S11 and S12 (SI) for different values of Γ. From both figures, it is evident that the debonding force increases with increasing path diameter, while the debonding stretch (or debonding displacement) decreases with patch diameter (where the adhesive thickness is constant t = 20 μm). We also derive the powerlaw for both the tapes (6A and 6B) based on our simulation as reported in Fig. 13 and 14 as a function of fracture energy Γ. We can compare it with an experimental investigation in the literature. According to the experimental study by Duigou-Majumdar *et al.*,[35] fibril debonding force should increase with the patch diameter as a power law of exponent 2.5, while the debonding stretch should increase with the patch diameter as a power law of exponent 0.5 while the present model predict that the debonding force for the custom PSA tapes (6A and 6B,

Table 3 Parameter for simulations for the different strain rate using Yeoh model

Fit parameters				
Name	Strain rate (S^{-1})	C_1	C_2	C_3
PSA type 6A	2	0.034 MPa	0.0011 MPa	0.000020 MPa
PSA type 6A	1	0.018 MPa	0.00021 MPa	2.4×10^{-6} MPa
PSA type 6A	0.2	0.0082 MPa	0.00012 MPa	1.2×10^{-6} MPa
PSA type 6A	0.01	0.0074 MPa	0.00011 MPa	1.2×10^{-6} MPa
PSA type 6B	2	0.034 MPa	0.0024 MPa	0.00012 MPa
PSA type 6B	1	0.019 MPa	−0.00013 MPa	4.01×10^{-6} MPa
PSA type 6B	0.2	0.020 MPa	0.00095 MPa	3.5×10^{-5} MPa
PSA type 6B	0.01	0.0064 MPa	-3.17×10^{-5} MPa	1.44×10^{-6} MPa

Table 4 Parameter for simulations: Yeoh Model, PSA tape 6A and PSA tape 6B

Name	C_1	C_2	C_3	$D_1 = D_2 = D_3$
PSA tape 6A				
Soft layer	0.034 MPa	0.0011 MPa	0.000020 MPa	6×10^{-1} MPa^{-1}
Rigid backing and substrate	0.5 GPa	−0.024 GPa	0.0017 GPa	0.04 GPa^{-1}
PSA tape 6B				
Soft layer	0.034 MPa	0.0024 MPa	0.00012 MPa	6×10^{-1} MPa^{-1}
Rigid backing and substrate	0.5 GPa	−0.024 GPa	0.0017 GPa	0.04 GPa^{-1}

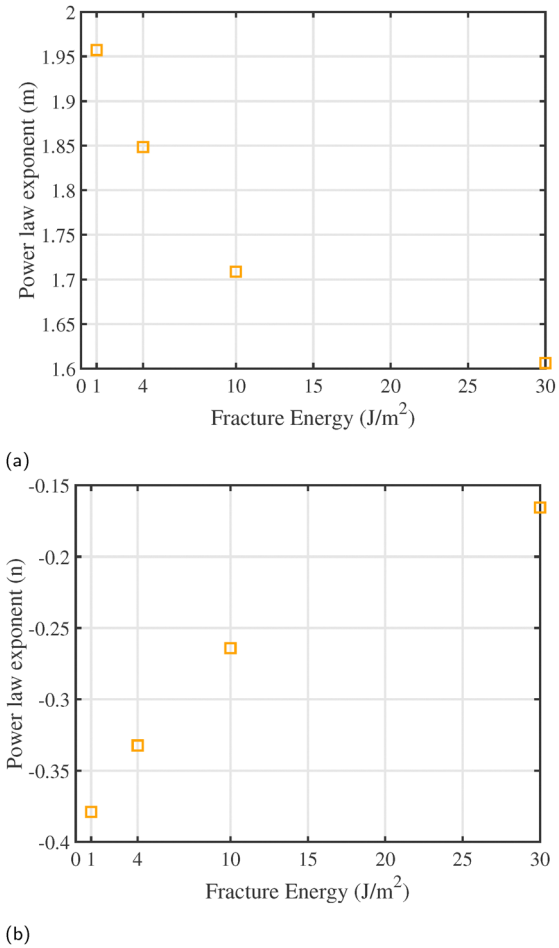

Fig. 13 PSA tape 6A, t = 20 μm, Φ = 5% (a) debonding force: $F_c \propto d^m$, where m depends on the fracture energy value used to derive the power law. It tells that the debonding force increases with the patch diameter with the positive power law exponent m (b) debonding displacement: $\delta_c \propto d^n$, where n depends on the fracture energy value used to derive the power law. It tells that the debonding displacement decreases with the patch diameter with the negative power law exponent n.

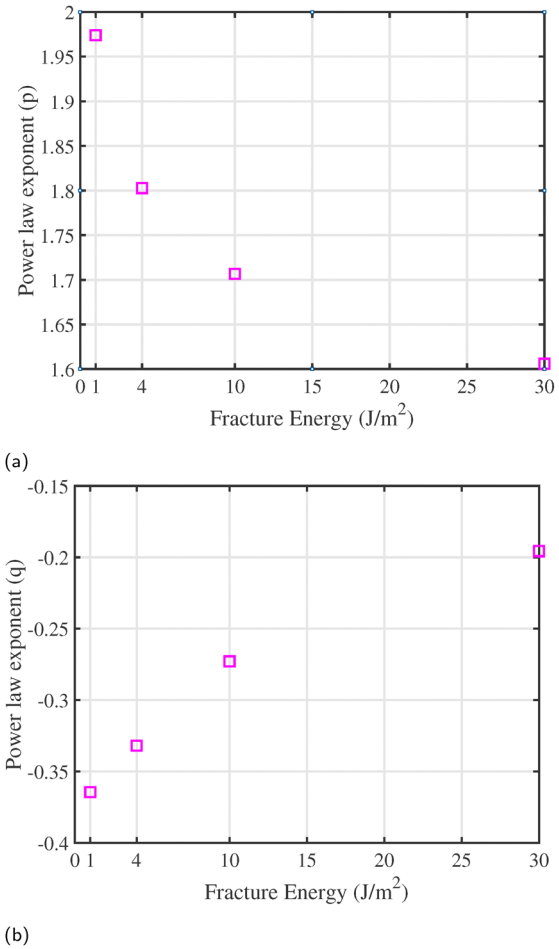

Fig. 14 PSA tape 6B, t = 20 μm, Φ = 5% (a) debonding force: $F_c \propto d^p$ where p is a function of fracture energy value used to derive the power law. It tells that the debonding force increases with the patch diameter with the positive power law exponent p (b) debonding displacement: $\delta_c \propto d^q$, where q is a function of fracture energy value used to derive the power law. It tells that the debonding displacement decreases with the patch diameter with the negative power law exponent q.

adjusted by the Yeoh model) should increase with the patch diameter as a power law of exponent between 1.6 to 2 based on Γ, while the debonding stretch should decrease with the patch diameter as a power law with negative exponent between −0.4 and −0.16 based on Γ value (*i.e.* for PSA 6A: $F_c \propto d^m$ and $\delta_c \propto d^n$ and for PSA 6B: $F_c \propto d^p$ and $\delta_c \propto d^q$ where m, n, p and q are given in Fig. 13 and 14). In Fig. S13 (SI), we show the effect of varying the adhesive's compressibility parameter D on the J-integral curves as a function of stretch. This allows predicting that for the constant fracture energy Γ, incompressible fibrils will debond earlier than more compressible fibrils.

4 Summary and discussion

We carried out the simulation of mono-fibril and checked the effect of changing geometric and material parameters on the nonlinear elastic response of fibril. We explored the impact of aspect ratios, inter-fibrillar distance, bulk modulus and strain-hardening. Finally, we discussed the powerlaw for fibril debonding and its variability based on the chosen fracture energy value.

Simulation confirms that the force to draw fibrils from a flat soft adhesive film is larger than the force required to uniaxially extend hypothetical independent strands of the adhesive. That is the reason why we see the "factor of 5" in the work by Chopin *et al.*[10] It means peeling energy is 5 times more than uniaxially extending a PSA tape in the rheometer. We explain the force *vs.* stretch graph for the different aspect ratios of the simulated fibril which is normalized by uniaxial stretching of the fibril by scaling models. We also discussed the impact of changing strain hardening, inter-fibriller distance and bulk modulus on the normalized force required to pull the fibril. Our hyperelastic simulation allows the definition of a fibril debonding criteria based on critical energy release rate (evaluated by the J-integral) that provides a valuable candidate to predict the debonding stretch of fibrils, which is the most important

missing ingredient for a predictive modeling of the peeling energy. Based on this model we could predict that the debonding force for the custom PSA tapes (6A and 6B, adjusted by the Yeoh model) should increase with the patch diameter as a power law of exponent m and p, while the debonding stretch should decrease with the patch diameter as a power law with negative exponent n and q respectively (*i.e.* $F_c \propto d^m$ and $\delta_c \propto d^n$ for PSA 6A and $F_c \propto d^p$ and $\delta_c \propto d^q$ for PSA 6B). While experimental study by Duigou-Majumdar *et al.*[35] suggest that fibril debonding force should increase with the patch diameter as a power law of exponent 2.5, while the debonding stretch should increase with the patch diameter as a power law of exponent 0.5 (*i.e.* $F_c \propto d^{5/2}$ and $\delta_c \propto d^{1/2}$). This discrepancy may be due to different tapes used in the experiment[35] and our simulation. Moreover, in the simulation, we did not consider the viscoelasticity. In the future extension of this work, we would like to use viscoelastic models in place of hyperelastic models.

Author contributions

Krupal Patel: writing – original draft, visualization, validation, investigation, formal analysis. Etienne Barthel: writing – review & editing, supervision, project administration, funding acquisition. Matteo Ciccotti: writing – review & editing, supervision, project administration, funding acquisition.

Conflicts of interest

There are no conflicts to declare.

Data availability

Data for this article is available in the manuscript itself. All material parameters are listed in Tables and one can use that to reproduce the FEM simulations in ABAQUS or any other finite element software.

The supplementary information provides additional details on the mesh-objectivity analysis, including mesh refinement and convergence studies. See DOI: https://doi.org/10.1039/d5sm00869g.

Appendix

A Appendix

Here, we give the derivation of W_{fibril} as per eqn (9). In the geometry of Fig. 7a, we can express the shear strain as follows:

$$\varepsilon_{\text{shear}} \sim \frac{\partial u_r}{\partial z} \tag{A.1}$$

$$\sim \frac{a(1-\lambda_a)}{\lambda_z t} \tag{A.2}$$

$$= \frac{a}{t}\left[\frac{1}{\lambda_z} - \frac{1}{\lambda_z^{3/2}}\right] \tag{A.3}$$

where, $\lambda_z = \lambda$, $\lambda_a = \lambda_\theta = \frac{1}{\sqrt{\lambda}}$ because the material is incompressible. From Fig. 7a, one can write the deformation gradient using the cylindrical co-ordinate as per below:

$$\underline{\underline{F}} = \begin{bmatrix} 1+\frac{\partial u_r}{\partial R} & \frac{1}{R}\frac{\partial u_r}{\partial \theta} - \frac{u_\theta}{R} & \frac{\partial u_r}{\partial z} \\ \frac{\partial u_\theta}{\partial R} & 1+\frac{1}{R}\frac{\partial u_\theta}{\partial \theta} - \frac{u_r}{R} & \frac{\partial u_\theta}{\partial z} \\ \frac{\partial u_z}{\partial R} & \frac{1}{R}\frac{\partial u_z}{\partial \theta} & 1+\frac{\partial u_z}{\partial z} \end{bmatrix} \tag{A.4}$$

$$\underline{\underline{F}} = \begin{bmatrix} \lambda_a & 0 & \frac{a}{t}\left[\frac{1}{\lambda_z} - \frac{1}{\lambda_z^{3/2}}\right] \\ 0 & \lambda_a & 0 \\ 0 & 0 & \lambda_z \end{bmatrix} \tag{A.5}$$

Now, the Green–Lagrange strain tensor is given by $\underline{\underline{E}} = \frac{1}{2}\left[\underline{\underline{F}}^T\underline{\underline{F}} - \underline{\underline{I}}\right]$

$$\underline{\underline{E}} = \begin{bmatrix} \lambda_a^2 - 1 & 0 & \lambda_a\frac{a}{t}\left[\frac{1}{\lambda_z} - \frac{1}{\lambda_z^{3/2}}\right] \\ 0 & \lambda_a^2 - 1 & 0 \\ \lambda_a\frac{a}{t}\left[\frac{1}{\lambda_z} - \frac{1}{\lambda_z^{3/2}}\right] & 0 & \lambda_z^2 + \frac{a^2}{t^2}\left[\frac{1}{\lambda_z} - \frac{1}{\lambda_z^{3/2}}\right]^2 - 1 \end{bmatrix} \tag{A.6}$$

If V is the volume of the elastomer, then W_{fibril} is given by

$$W_{\text{fibril}} \sim \mu \,\text{trace}\left(\underline{\underline{E}}\right) V \tag{A.7}$$

$$W_{\text{fibril}} \sim a^2 t\mu\left[\lambda_z^2 + \frac{2}{\lambda_z} + \frac{a^2}{t^2}\left[\frac{1}{\lambda_z} - \frac{1}{\lambda_z^{3/2}}\right]^2 - 3\right] \tag{A.8}$$

The derivation of the expression for force is given as follows.

$$F = \frac{\partial W}{\partial \delta} \tag{A.9}$$

$$F = \frac{1}{t}\frac{\partial W}{\partial \lambda} \tag{A.10}$$

$$F_{\text{fibril}} \sim a^2\mu\left[2\lambda_z - \frac{2}{\lambda_z^2} + \frac{2a^2}{t^2}\left[\frac{1}{\lambda_z} - \frac{1}{\lambda_z^{3/2}}\right]\left[\frac{3}{2\lambda_z^{5/2}} - \frac{1}{\lambda_z^2}\right]\right] \tag{A.11}$$

$$F_{\text{uniaxial}} \sim a^2\mu\left[2\lambda_z - \frac{2}{\lambda_z^2}\right] \tag{A.12}$$

when we put $\lambda_z = 1 + \frac{\delta}{t}$ in the eqn (A.11) and consider the small strain limit by neglecting the higher order terms ($\lambda_z^{5/2}$ and $\lambda_z^{3/2}$), we would recover the force equation given by the poker chip model.

Acknowledgements

"This project has received funding from the European Union's Horizon 2020 research and innovation program under the Marie Skłodowska-Curie grant agreement no. 754387". We are grateful to the funding agency. The authors thank the

UpToParis program at ESPCI Paris for providing administrative help throughout this project. The authors also thank Xavier Morelle and Bruno Bresson for providing the SEM image of the adhesion rupture of the PSA tape on a patterned substrate. We would also like to thank the reviewers for their helpful comments in improving this manuscript.

References

1 M. Barquins and M. Ciccotti, *Int. J. Adhes. Adhes.*, 1997, **17**, 65–68.
2 D. Kaelble, *Trans. Soc. Rheol. IV*, 1960, **4**, 45–73.
3 R. S. Rivlin and A. G. Thomas, *J. Polym. Sci.*, 1953, **12**, 291–318.
4 J. Ferry, *Viscoelastic properties of polymers*, Wiley, New York, 1970.
5 A. Gent and R. Petrich, *Proc. R. Soc. London, Ser. A*, 1969, **310**, 433–448.
6 E. Andrews and A. Kinloch, *J. Polym. Sci., Polym. Symp.*, 1974, **46**, 1–14.
7 D. Kaelble, *J. Colloid Sci.*, 1964, **19**, 413–424.
8 D. Maugis, *J. Mater. Sci.*, 1985, **20**, 3041–3073.
9 R. Villey, P.-P. Cortet, C. Creton, M. Ciccotti, M.-J. Dalbe, T. Jet, B. Saintyves, S. Santucci, V. Loic and D. Yarusso, *Soft Matter*, 2015, **11**, 3480.
10 J. Chopin, R. Villey, D. Yarusso, E. Barthel, C. Creton and M. Ciccotti, *Macromolecules*, 2018, **51**, 8605–8610.
11 R. Villey, P.-P. Cortet, C. Creton and M. Ciccotti, *Int. J. Fract.*, 2017, **204**, 175–190.
12 P.-G. de Gennes, *C. R. Seances Acad. Sci., Ser. 2*, 1988, **307**, 1949–1953.
13 B. Persson, O. Albohr, G. Heinrich and H. Ueba, *J. Phys.: Condens. Matter*, 2005, **17**, R1071.
14 A. Gent, *Langmuir*, 1996, **12**, 4492–4496.
15 C. Creton, *MRS Bull.*, 2003, **28**, 434–439.
16 C. Creton and M. Ciccotti, *Rep. Prog. Phys.*, 2016, **79**, 046601.
17 A. Crosby and K. Shull, *J. Polym. Sci., Part B: Polym. Phys.*, 1999, **37**, 3455–3472.
18 A. Zosel, *Colloid Polym. Sci.*, 1985, **263**, 541–553.
19 H. Lakrout, P. Sergot and C. Creton, *J. Adhes.*, 1999, **69**, 307–359.
20 A. Lindner, B. Lestriez, S. Mariot, T. Maevis, R. Brummer, B. Luehmann and C. Creton, *J. Adhes.*, 2006, **82**, 267.
21 F. Tanguy, M. Nicoli, A. Lindner and C. Creton, *Eur. Phys. J. E: Soft Matter Biol. Phys.*, 2014, **37**, 3.
22 T. Yamaguchi, K. Koike and M. Doi, *Europhys. Lett.*, 2007, **77**, 64002.
23 A. Zosel, *Int. J. Adhes. Adhes.*, 1998, **18**, 265.
24 N. Wyatt and A. Grillet, *J. Appl. Polym. Sci.*, 2014, **131**, 40034.
25 C. Creton, J. Hooker and K. Shull, *Langmuir*, 2001, **17**, 4948–4954.
26 J. Teisseire, F. Nallet, P. Fabre and C. Gay, *J. Adhes.*, 2007, **83**, 613.
27 J. Dollhofer, A. Chiche, V. Muralidharan, C. Creton and Y. Hui, *Int. J. Solids Struct.*, 2004, **41**, 6111.
28 K. Foteinopoulou, V. Mavrantzas, Y. Dimakopoulos and J. Tsamopoulos, *Phys. Fluids*, 2006, **18**, 042106.
29 T. Yamaguchi and M. Doi, *Eur. Phys. J. E: Soft Matter Biol. Phys.*, 2006, **21**, 331.
30 J. Papaioannou, A. Giannousakis, Y. Dimakopoulos and J. Tsamopoulos, *Ind. Eng. Chem. Res.*, 2014, **53**, 7548.
31 J. Pelfrene, S. Van Dam and W. Van Paepegem, *Int. J. Adhes. Adhes.*, 2015, **62**, 146–153.
32 S. Lin, Y. Mao, R. Radovitzky and X. Zhao, *J. Mech. Phys. Solids*, 2017, **106**, 229–256.
33 S. Varchanis, A. Kordalis, Y. Dimakopoulos and J. Tsamopoulos, *Phys. Rev. Fluids*, 2021, **6**, 013301.
34 V. R. Krishnan and C.-Y. Hui, *Soft Matter*, 2008, **4**, 1909–1915.
35 A. Duigou-Majumdar, P.-P. Cortet and C. Poulard, *Soft Matter*, 2022, **18**, 5857–5866.
36 E. M. Arruda and M. C. Boyce, *J. Mech. Phys. Solids*, 1993, **41**, 389–412.
37 O. H. Yeoh, *Rubber Chem. Technol.*, 1990, **63**, 792–805.
38 T. Sussman and K. Bathe, *J. Comput. Struct.*, 1987, **26**, 357–409.
39 K. Patel, E. Barthel and M. Ciccotti, *Eng. Anal. Bound Elem.*, 2025, **177**, 106259.
40 Y. Sugizaki, T. Shiina, Y. Tanaka and A. Suzuki, *J. Adhes. Sci. Technol.*, 2016, **30**, 2637–2654.

